PCCP

PAPER

View Article Online
View Journal | View Issue



Cite this: *Phys. Chem. Chem. Phys.*, 2024, **26**, 26585

# Selected ion flow tube studies of the reactions of $H_3O^+$, $NO^+$, $O_2^{+\bullet}$ and $O^{-\bullet}$ ions with alkanes in He and $N_2$ carrier gases at different temperatures†

Maroua Omezzine Gnioua, [ab] Stefan J. Swift [a] and Patrik Španěl *[a]

Received 6th August 2024,
Accepted 6th October 2024

DOI: 10.1039/d4cp03105a

rsc.li/pccp

The kinetics of the reactions of $H_3O^+$, $NO^+$, $O_2^{+\bullet}$ and $O^{-\bullet}$ with *n*-hexane, 3-methylpentane, 2,5-dimethylhexane and 2,3-dimethylheptane were studied experimentally under several selected ion flow tube (SIFT) conditions: in a Profile 3 instrument in He and $N_2$ carrier gases at 300 K and in the Voice200 instrument in $N_2$ carrier gas at 300 and 393 K – where the effect of the extraction lens voltage was also assessed. It was found that $H_3O^+$ ions react differently than expected, with reaction rates slower than collisional. Instead of transferring a proton, they associate and form fragment product ions $[M-H]^+$. $NO^+$ ions react *via* hydride ion transfer. $O_2^{+\bullet}$ ions react *via* charge transfer followed by fragmentation that is highly sensitive to the temperature and the ion extraction lens voltage. Negative ions did not react, except for the $O^{-\bullet}$ ion, which reacted *via* an associative detachment process. Computational analysis using Density Functional Theory (DFT) provided insights into the exothermicities and exergodicities of these reactions. A notable result is that proton transfer from $H_3O^+$ does not take place despite its potential exothermicity; this is important for the interpretation of proton transfer reaction (PTR) and SIFT mass spectrometry data.



## 1. Introduction

Selected ion flow tube mass spectrometry (SIFT-MS) is being increasingly used as a highly sensitive and rapid soft chemical ionisation technique for analysing gaseous matrices.[1] It has been widely used in recent years for environmental studies,[2,3] headspace analyses of foods,[4] breath analyses within clinical settings,[5] headspace analyses of archaeological artefacts[6,7] as well as for investigating ion–molecule reactions.[1]

In SIFT-MS, several reagent ions for the chemical ionisation of analyte species can be switched rapidly.[1,8] In recent years, the selection of possible reagent ions for analyses has expanded from traditional three ($H_3O^+$, $NO^+$ and $O_2^{+\bullet}$) to eight by including five negative ($OH^-$, $O_2^{-\bullet}$, $O^{-\bullet}$, $NO_2^-$ and $NO_3^-$).[9]

To date, the analysis of alkanes using selected ion flow tube mass spectrometry (SIFT-MS) remains challenging. Despite this, alkanes play a critical role in atmospheric chemistry, environmental analysis,[10,11] and clinical volatolomics.[12–16] Thus, to facilitate SIFT-MS alkane analyses, the ion chemistry needs to be understood in detail.

We investigated the ion–molecule reactions between representative alkanes and the SIFT-MS reagent ions in He and $N_2$ carrier gases at 300 K and 393 K. The study included three branched alkanes relevant to disease diagnostics:[16] 3-methylpentane, 2,5-dimethylhexane, 2,3-dimethylheptane and the straight-chain alkane *n*-hexane (the isomer of 3-methylpentane), for comparison (Fig. 1). The energetics of the observed reactions were calculated using density functional theory (DFT) calculations.

## 2. Experimental

The SIFT-MS technique has been detailed in previous articles.[8,17–21] In brief, plasma produced in the ion source is filtered by a quadrupole mass filter to select a single type of reagent ion. The gaseous sample is introduced into the flow tube with a carrier gas (He or $N_2$), where ion–molecule reactions occur with neutral molecules during a defined time at pressures below 1 torr. The quadrupole mass spectrometer then analyses the reagent and product ions.

### 2.1. Materials and instruments

This study used the standard reagents *n*-hexane (≥99%, Sigma-Aldrich, Steinheim, Germany), 3-methylpentane (≥99%, Sigma-Aldrich, St Louis MO, USA), 2,5-dimethylhexane

[a] *J Heyrovský Institute of Physical Chemistry of the CAS, v. v. i., Dolejškova 2155/3, 182 23 Prague 8, Czechia. E-mail: patrik.spanel@jh-inst.cas.cz*
[b] *Faculty of Mathematics and Physics, Charles University, V Holešovičkách 2/747, Prague 8, 180 00, Czechia*

† Electronic supplementary information (ESI) available. See DOI: https://doi.org/10.1039/d4cp03105a

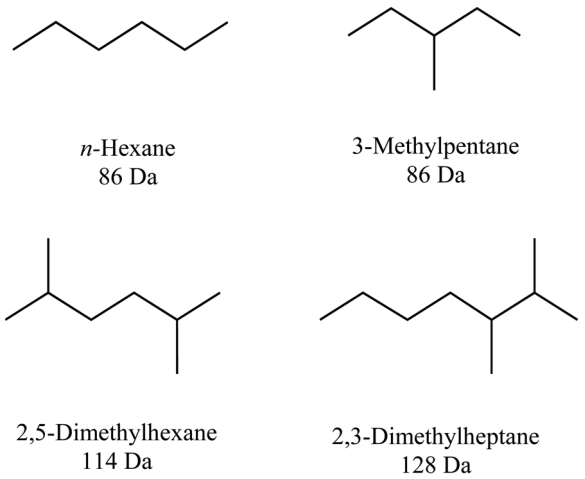


Fig. 1 Skeletal structures, names and relative molecular masses (RMM) of the four alkane species investigated in this work.

(99%, Sigma-Aldrich, St Louis MO, USA), and 2,3-dimethylheptane (98%, Sigma-Aldrich, St Louis MO, USA).

A Voice200infinity SIFT-MS instrument (Syft Technologies™, Christchurch, New Zealand) was used with positive reagent ions ($H_3O^+$, $NO^+$ and $O_2^{+\bullet}$) and negative reagent ions ($O^{-\bullet}$, $NO_2^-$, $NO_3^-$, $OH^-$ and $O_2^{-\bullet}$). The flow tube temperature was either ambient (300 ± 3 K) or stabilised at 120 °C (393 K) at a flow tube pressure of 470 mTorr, using $N_2$ (purity 5.0, Messer Technogas, Prague, Czechia) as the carrier gas. For some experiments, the voltage of the ion extraction lens (LE) at the entrance of the downstream mass spectrometer was lowered from the standard 7 V to 4 V, to minimise fragmentation. Alkane vapour samples diluted by zero air were introduced into the flow tube *via* a heated sampling inlet at a standard flow rate of 25 sccm. To monitor the formation of free electrons as products of negative ion reactions, a 1 sccm flow rate of 1% $SF_6$ in $N_2$ was introduced in addition to the alkane vapour samples. Formation of $SF_6^-$ was considered to indicate the presence of free electrons.

An earlier model of the SIFT-MS instrument, the Profile 3 (Instrument Science Crewe, United Kingdom), was used with positive reagent ions ($H_3O^+$, $NO^+$ and $O_2^{+\bullet}$) at an ambient flow tube temperature of 300 K. Helium (920 mTorr) and nitrogen (200 mTorr) were used as carrier gases (He purity of 4.6, $N_2$ purity of 5.0, Messer Technogas, Prague). Alkane vapour samples diluted by zero air were introduced into the flow tube *via* a heated capillary at a flow rate of 25 sccm.

### 2.2. Experiments to determine branching ratios and relative rate coefficients

Clean zero-air was introduced at a flow rate of 200 sccm into a glass bottle, from which 25 sccm was sampled into the SIFT-MS instruments. Full scan mass spectra were repeatedly obtained in the mass-to-charge ($m/z$) range of 10 to 250 for the positive reagent ions (1 minute for each scan); the appropriate volume of alkane headspace was injected into the glass bottle; and the vapour concentration was allowed to decrease over a time of 20 minutes. The decrease in reagent ion signal was observable immediately after vapour injection and the main product ion signals were typically reduced in intensity from $>10^5$ c $s^{-1}$ to $<10^4$ c $s^{-1}$.

Product ion branching ratios and relative rate coefficients of reactions of different reagent ions with the same neutral compound were determined using an algorithm implemented in Python. First, the raw experimental data were parsed and compiled into a peak table listing ion count rates for all reagent ions registered at different times. The process then involves selecting the 20 most intense signals from the raw data (based on the average count rate over the entire experiment). Thus, no assumptions or manual choices were made concerning the selection of the product ions. These ions include the injected reagent ions, background signals, and the dominant product ions produced by the reactions. In the next step, the product ions were identified based on the decrease in signal intensity after introducing the reactant vapour. The background was then determined by extrapolating the ion count rates to the later time when the reactant vapour almost disappeared. To estimate the concentration of the neutral reactant molecules ($M$), the ratio of background-corrected reagent to product ion signal ($R/P$) was used to provide an indirect measure of the concentration of $M$ as

$$[M] = \ln\left(1 + \frac{P}{R}\right) \quad (1)$$

The algorithm plotted the percentage of each product ion signal as a function of $[M]$ to understand how the product ion distribution varied with $[M]$. Subsequently, parabolic curves were used to model the dependence of product ion percentages on concentration, allowing for primary and secondary ion products to be distinguished. The secondary products, with intercept values < 1%, were excluded from subsequent analysis to determine true primary product ion branching ratios. Subsequently, a linear fit was applied to the data, and branching ratios were taken as the intercept when extrapolating to the limit of $[P]/[R]$ (and thus $[M]$) approaching zero. $^{13}C$ isotopologues of the main product ions were used to confirm the number of carbon atoms.[22]

Relative rate coefficients were determined by analysing changes in ion signals with varying concentrations, $M$, considering both the decrease in reagent ion signals and the increase in total product ion signals. The theoretical collisional rate coefficients ($k_c$) were calculated using the Su and Chesnavich method.[23] The relative rates were then multiplied by $k_c$ for the fastest observed reaction. This gave the resulting experimental rate coefficient ($k$).

### 2.3. DFT calculations

DFT calculations were conducted to evaluate the thermodynamics of the investigated reactions, which would confirm the presence of a specific branching pathway. All quantum chemistry calculations were performed using the ORCA 5.0.4 software.[24] Molecular geometries of all neutral reactant

 

molecules and of all reagent and product ions were first drawn using the AVOGADRO software and then further optimised using ORCA, with the B3LYP DFT and the 6-311++G(d,p) basis set with D4 correction.[25] This basis set has been recently validated on multiple calculations related to ion energetics and kinetics.[26,27] This level of theory was also used to calculate the normal mode vibrational frequencies and the total enthalpies, entropies and Gibbs free energies of the neutral molecules (including their polarizabilities and dipole moments). Thermodynamic values were calculated for selected observed product ions along with their corresponding neutral products. From these, the changes in enthalpies ($\Delta H$) and Gibbs free energies ($\Delta G$) were calculated for the reactions discussed later.[28] Expected proton affinities (PA) for several potential protonated structures were calculated as the difference between the total enthalpies of the neutral molecules and the various optimised protonated structures, accounting for the thermal enthalpy of a free proton of 6.2 kJ mol$^{-1}$ at 298.15 K.[28,29]

# 3. Results and discussion

Table 1 gives the product ions identified for the reactions of all available reagent ions with *n*-hexane, 3-methylpentane, 2,5-dimethylhexane and 2,3-dimethylpentane, together with the branching ratios of the reactions observed using the Voice200infinity instrument ($N_2$ carrier gas, 300 K, 4 V at the ion extraction lens LE – data for 393 K at 4 and 7 V are in Tables S1 and S2 in ESI†). Corresponding data for product ions observed in the Profile 3 instrument (He and $N_2$ carrier gases at 300 K) are summarised in Table 2.

Table 3 gives the reaction rate coefficients obtained in the Voice200, together with the molecular properties used for their calculation. The Profile 3 results are given in Table 4.

## 3.1. Positive ions

**3.1.1. $H_3O^+$ reactions.** It is commonly expected that $H_3O^+$ reagent ions will react with organic molecules by proton transfer, resulting in $MH^+$ ions, as long as the molecules' proton affinities are greater than those of $H_2O$ (691 kJ mol$^{-1}$).[32] It is thus a striking result that $MH^+$ ions (expected at *m*/*z* 87, 115, and 129) are not observed amongst the product ions, in agreement with previous work on small hydrocarbons.[33]

The main ion product for *n*-hexane, $C_6H_{14}$, is the adduct ion observed at *m*/*z* 105 that undergoes a fast secondary reaction with $H_2O$ molecules forming $H_3O^+{\cdot}H_2O$ at *m*/*z* 37. Another product ion is $(M–H)^+$ at *m*/*z* 85, resulting from the formation of $H_2$ from the transient reaction complex ($C_6H_{14}{\cdot}H_3O^+$*). In the Voice200, an ion product $C_5H_{11}^+$at *m*/*z* 71 is also present, corresponding to the formation of a $CH_4$ molecule.

$$H_3O^+ + C_6H_{14} \xrightarrow{He,N_2} C_6H_{14}\cdot H_3O^+ \ (m/z\ 105) \quad (2a)$$

$$\rightarrow C_6H_{13}^+ + H_2 + H_2O \quad (m/z\ 85) \quad (2b)$$

$$\rightarrow C_5H_{11}^+ + CH_4 + H_2O \quad (m/z\ 71) \quad (2c)$$

Table 1 Product ions for the reactions of the reagent ions with the alkanes observed using the Voice200infinity with a $N_2$ carrier gas at a flow tube temperature of 300 K at 4 V with an LE lens. The relative molecular mass of the alkanes is shown in parentheses after the alkane name; for the product ions, the *m*/*z* value of the product ion is shown first, followed by the formula and the branching ratio in parentheses

| Compound (RMM/Da) | $H_3O^+$ | $NO^+$ | $O_2^{+\bullet}$ |
|---|---|---|---|
| *n*-Hexane (86)<br>$C_6H_{14}$ | 105 $C_6H_{14}{\cdot}H_3O^+$ (70)<br>85 $C_6H_{13}^+$ (16) 71 $C_5H_{11}^+$ (14) | 116 $C_6H_{14}{\cdot}NO^+$ (18)<br>85 $C_6H_{13}^+$ (67)<br>83 $C_6H_{11}^+$ (15) | 57 $C_4H_9^+$ (39)<br>56 $C_4H_8^{+\bullet}$ (25)<br>86 $C_6H_{14}^{+\bullet}$ (24)<br>42 $C_3H_6^{+\bullet}$ (6)<br>43 $C_3H_7^+$ (6) |
| 3-Methylpentane (86)<br>$C_6H_{14}$ | 105 $C_6H_{14}{\cdot}H_3O^+$ (45)<br>85 $C_6H_{13}^+$ (44)<br>71 $C_5H_{11}^+$ (11) | 85 $C_6H_{13}^+$ (100) | 56 $C_4H_8^{+\bullet}$ (57)<br>57 $C_4H_9^+$ (31)<br>86 $C_6H_{14}^{+\bullet}$ (6)<br>55 $C_4H_7^+$ (3)<br>71 $C_5H_{11}^+$ (3) |
| 2,5-Dimethylhexane (114)<br>$C_8H_{18}$ | 133 $C_8H_{18}{\cdot}H_3O^+$ (64)<br>113 $C_8H_{17}^+$ (36) | 113 $C_8H_{17}^+$ (100) | 99 $C_7H_{15}^+$ (29)<br>57 $C_4H_9^+$ (23)<br>114 $C_8H_{18}^{+\bullet}$ (15)<br>71 $C_5H_{11}^+$ (11)<br>70 $C_5H_{10}^{+\bullet}$ (7)<br>112 $C_8H_{16}^{+\bullet}$ (4)<br>42 $C_3H_7^+$ (6)<br>43 $C_3H_7^+$ (3)<br>56 $C_4H_8^{+\bullet}$ (2) |
| 2,3-Dimethylheptane (128)<br>$C_9H_{20}$ | 147 $C_9H_{20}{\cdot}H_3O^+$ (12)<br>127 $C_9H_{19}^+$ (88) | 127 $C_9H_{19}^+$ (100) | 84 $C_6H_{12}^{+\bullet}$ (48)<br>85 $C_6H_{13}^+$ (31)<br>128 $C_9H_{20}^{+\bullet}$ (7)<br>71 $C_5H_{11}^+$ (7)<br>70 $C_5H_{10}^{+\bullet}$ (3)<br>56 $C_4H_8^{+\bullet}$ (2)<br>83 $C_6H_{11}^+$ (2) |

Table 2 Branching ratios for the product ions of the alkane reactions observed in the Profile 3 with a He and $N_2$ carrier gas at 300 K. The relative molecular mass of the alkanes is shown in parentheses after the alkane name; for the product ions, the *m*/*z* value of the product ion is shown first, followed by the formula and the branching ratio in parentheses

| | He carrier gas | | | $N_2$ carrier gas | | |
|---|---|---|---|---|---|---|
| Compound (RMM/Da) | $H_3O^+$ | $NO^+$ | $O_2^{+\bullet}$ | $H_3O^+$ | $NO^+$ | $O_2^{+\bullet}$ |
| *n*-Hexane (86)<br>$C_6H_{14}$ | 105 $C_6H_{14}{\cdot}H_3O^+$ (96)<br>85 $C_6H_{13}^+$ (4) | 116 $C_6H_{14}{\cdot}NO^+$ (12)<br>85 $C_6H_{13}^+$ (88) | 86 $C_6H_{14}^{+\bullet}$ (38)<br>85 $C_6H_{13}^+$ (4)<br>57 $C_4H_9^+$ (35)<br>56 $C_4H_8^{+\bullet}$ (21)<br>55 $C_4H_7^+$ (2) | 105 $C_6H_{14}{\cdot}H_3O^+$ (91)<br>85 $C_6H_{13}^+$ (9) | 116 $C_6H_{14}{\cdot}NO^+$ (1)<br>85 $C_6H_{13}^+$ (85)<br>83 $C_6H_{11}^+$ (14) | 86 $C_6H_{14}^{+\bullet}$ (36)<br>85 $C_6H_{13}^+$ (6)<br>57 $C_4H_9^+$ (31)<br>56 $C_4H_8^{+\bullet}$ (24)<br>55 $C_4H_7^+$ (3) |
| 3-Methylpentane (86)<br>$C_6H_{14}$ | 105 $C_6H_{14}{\cdot}H_3O^+$ (42)<br>85 $C_6H_{13}^+$ (58) | 85 $C_6H_{13}^+$ (100) | 86 $C_8H_{18}^{+\bullet}$ (18)<br>57 $C_4H_9^+$ (31)<br>56 $C_4H_8^{+\bullet}$ (51) | 105 $C_6H_{14}{\cdot}H_3O^+$ (33)<br>85 $C_6H_{13}^+$ (67) | 85 $C_6H_{13}^+$ (100) | 86 $C_8H_{18}^{+\bullet}$ (15)<br>57 $C_4H_9^+$ (27)<br>56 $C_4H_8^{+\bullet}$ (52)<br>55 $C_4H_7^+$ (6) |
| 2,5-Dimethylhexane (114)<br>$C_8H_{18}$ | 133 $C_8H_{18}{\cdot}H_3O^+$ (74)<br>113 $C_8H_{17}^+$ (26) | 113 $C_8H_{17}^+$ (100) | 114 $C_8H_{18}^{+\bullet}$ (24)<br>113 $C_8H_{17}^+$ (3)<br>112 $C_8H_{16}^{+\bullet}$ (3)<br>99 $C_7H_{15}^+$ (35)<br>71 $C_5H_{11}^+$ (11)<br>70 $C_5H_{10}^{+\bullet}$ (7)<br>57 $C_4H_9^+$ (14)<br>43 $C_3H_7^+$ (2) | 133 $C_8H_{18}{\cdot}H_3O^+$ (55)<br>113 $C_8H_{17}^+$ (45) | 113 $C_8H_{17}^+$ (100) | 114 $C_8H_{18}^{+\bullet}$ (24)<br>113 $C_8H_{17}^+$ (4)<br>112 $C_8H_{16}^{+\bullet}$ (3)<br>99 $C_7H_{15}^+$ (32)<br>71 $C_5H_{11}^+$ (14)<br>70 $C_5H_{10}^{+\bullet}$ (7)<br>57 $C_4H_9^+$ (14)<br>43 $C_3H_7^+$ (2) |
| 2,3-Dimethylheptane (128)<br>$C_9H_{20}$ | 147 $C_9H_{20}{\cdot}H_3O^+$ (10)<br>127 $C_9H_{19}^+$ (90) | 127 $C_9H_{19}^+$ (100) | 128 $C_9H_{20}^{+\bullet}$ (13)<br>85 $C_6H_{13}^+$ (33)<br>84 $C_6H_{12}^{+\bullet}$ (44)<br>83 $C_6H_{11}^+$ (2)<br>71 $C_5H_{11}^+$ (7)<br>56 $C_4H_8^{+\bullet}$ (1) | 147 $C_9H_{20}{\cdot}H_3O^+$ (8)<br>127 $C_9H_{19}^+$ (92) | 127 $C_9H_{19}^+$ (100) | 128 $C_9H_{20}^{+\bullet}$ (13)<br>85 $C_6H_{13}^+$ (29)<br>84 $C_6H_{12}^{+\bullet}$ (44)<br>83 $C_6H_{11}^+$ (6)<br>71 $C_5H_{11}^+$ (6)<br>56 $C_4H_8^{+\bullet}$ (2) |

Table 3 The experimentally derived reaction rate coefficients ($k$) and the theoretical collisional rate coefficients ($k_c$) (shown in square brackets) of the alkane reactions obtained in the Voice200infinity SIFT-MS in $N_2$ carrier gas at 300 K using a 4 V LE lens. The units of $k$ and $k_c$ are $10^{-9}$ $cm^3$ $s^{-1}$

| Voice200infinity | | | | | |
|---|---|---|---|---|---|
| Compound | Polarizability, $\alpha$ Å$^3$ ($\times 10^{-24}$ $cm^3$) | Dipole moment, $D$ debye | $H_3O^+$ $k$, [$k_c$] | $NO^+$ $k$, [$k_c$] | $O_2^{+\bullet}$ $k$, [$k_c$] |
| *n*-Hexane (86) 10.29[a] | 11.3[b] | 0.00[b] | 0.4, [2.0] | 0.0, [1.7] | 1.6, [1.6] |
| 3-Methylpentane (86) 10.04[a] | 11.2[b] | 0.10[b] | 0.6, [2.0] | 1.7, [1.7] | 1.4, [1.6] |
| 2,5-Dimethylhexane (114) 9.76[a] | 14.9[b] | 0.00[b] | 1.1, [2.2] | 1.8, [1.9] | 1.8, [1.8] |
| 2,3-Dimethylheptane (128) | 16.6[b] | 0.08[b] | 2.4, [2.4] | 1.6, [2.0] | 1.7, [2.0] |

[a] Ionisation energy values in eV obtained from the NIST database.[30] [b] DFT Calculations using the ORCA programme with the B3LYP DFT and 6-311++G(d,p) basis set, with a D4 correction.[31]

The branching ratios are different under different conditions. The association pathway is dominant in the Profile 3, in both carrier gases (over 90%). In the Voice200, the percentage of the adduct is 70% at 300 K, and disappears completely at 393 K. The signal intensities of $C_6H_{13}^+$ and $C_5H_{11}^+$ are similar in the Voice200, whilst in the Profile 3, the signal at *m*/*z* 71 is 20 times smaller than that at *m*/*z* 85, corresponding to less than 1% of the net reaction.

The results for the branched isomer, 3-methylpentane, are qualitatively similar; the main difference being that the net rate coefficients are faster and the channel forming $C_6H_{13}^+$ is always dominant in all observed conditions.

For the 2,5-dimethylhexane reaction, the main product at 300 K is the adduct ion, with $(M–H)^+$ corresponding to the formation of a neutral $H_2$ molecule.

$$H_3O^+ + C_8H_{18} \xrightarrow{He,N_2} C_8H_{18}\cdot H_3O^+ \quad (m/z\ 133) \tag{3a}$$

$$\rightarrow C_8H_{17}^+ + H_2 + H_2O \quad (m/z\ 113) \tag{3b}$$

At higher temperatures (393 K) the adduct branching ratio reduces from 14% to 7% depending on the ion optics voltage.

2,3-Dimethylheptane reacts with $H_3O^+$ mostly by producing the $(M–H)^+$ product, with only a minor adduct ion signal observed.

$$H_3O^+ + C_9H_{20} \rightarrow C_9H_{19}^+ + H_2 + H_2O\ (m/z\ 127) \tag{4a}$$

$$\xrightarrow{He,N_2} C_9H_{20}\cdot H_3O^+ \quad (m/z\ 147) \tag{4b}$$

 

Table 4 The experimentally derived reaction rate coefficients ($k$) and the theoretical collisional rate coefficients ($k_c$) (shown in square brackets) of the alkane reactions obtained in the Profile 3 SIFT-MS, in both He and $N_2$ carrier gases at 300 K. The rate coefficients shown in standard font are in He; rate coefficients in bold are in $N_2$ carrier gas. The units of $k$ and $k_c$ are $10^{-9}$ $cm^3$ $s^{-1}$

| Profile 3 at 300 K | | | |
|---|---|---|---|
| Compound | $H_3O^+$ $k$, **$k$**, [$k_c$] | $NO^+$ $k$, **$k$**, [$k_c$] | $O_2^{+\bullet}$ $k$, **$k$**, [$k_c$] |
| *n*-Hexane (86) | 0.5, **0.2**, [2.0] | 0.1, **0.7**, [1.7] | 1.6, **1.6**, [1.6] |
| 3-Methylpentane (86) | 0.9, **0.8**, [2.0] | 1.7, **1.7**, [1.7] | 1.4, **1.2**, [1.6] |
| 2,5-Dimethylhexane (114) | 1.7, **1.4**, [2.2] | 1.9, **1.9**, [1.9] | 1.4, **1.1**, [1.8] |
| 2,3-Dimethylheptane (128) | 2.0, **1.9**, [2.4] | 2.0, **2.0**, [2.0] | 2.0, **2.0**, [2.0] |

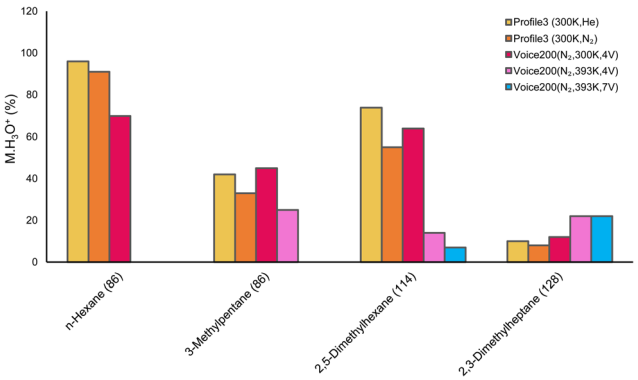


Fig. 2 The branching ratios of the association channels of $H_3O^+$ reactions with alkanes under various conditions.

At higher temperatures, the adduct remains a minor but significant ion product (~20%).

The bar chart in Fig. 2 illustrates the branching ratios of association channels for all compounds under various conditions.

To understand why protonated molecules ($MH^+$) are not observed, DFT calculations were performed to determine the geometries and enthalpies of protonated forms of each alkane molecule, considering several possible positions of $H^+$. Geometry optimisation revealed that the stable structures of protonated alkane molecules can be represented as $(M–H)^+$ $H_2$, $(M–CH_3)^+{\cdot}CH_4$, or $R_1H{\cdot}R_2^+$, where $R_1$ and $R_2$ are alkane fragment radicals. The geometries of these various protonated alkane formations are shown in Fig. 3.

PA values calculated for each of the structures shown in Fig. 3 are given in Table 5. Note that for each alkane species, at least one configuration corresponds to a proton affinity greater than that of water. Note that the structures indicate the composition of the ions from two units: a positively charged closed shell ion weakly bound to a neutral moiety $C_nH_{2n+2}$ ($n$ = 0...3). As the formation of $MH^+$ was not observed, it appears that they are not thermodynamically stable and dissociate into the observed product ions.

The experiments clearly reveal that the $H_3O^+$ reactions lead to the formation of $(M–H)^+$ product ions. To understand how the reactions (2b), (3b) and (4a) proceed, several possible structures of the $(M–H)^+$ product ions were optimised by DFT, and the lowest energy case was used to calculate the reaction enthalpy ($\Delta H$) and Gibbs Free energy ($\Delta G$) changes; the results are given in Table 6.

It is interesting to note that the reactions are close to thermoneutral, $\Delta H$, ranging from slightly exothermic ($-8$ kJ $mol^{-1}$) to endothermic (+13 kJ $mol^{-1}$). However, the calculations reveal that all these reactions are exergonic because the $\Delta G$ is negative. This is due to a significant increase in translational entropy caused by the ejection of separate $H_2$ and $H_2O$ molecules. The $T\Delta S$ term for an additional $H_2$ product molecule contributes $-37$ kJ $mol^{-1}$. The suggested mechanism of this reaction involves the formation of the $MH_3O^{+*}$ transitional complex, from which an $H_2$ molecule and an $H_2O$ molecule are ejected after the $(M–H)^+$ product ion is formed within this complex. Fig. 4. illustrates the mechanism for the formation of the $(M–H)^+$ product ion on an example of 3-methylpentane. Note that the $H_2$ molecule is formed from one of the H atoms of the $H_3O^+$ and from an H atom in the middle of the hydrocarbon molecule. This was validated by preliminary molecular dynamics simulations of this reaction using the ORCA MD module.

Considering the rate coefficients, the speed of $H_3O^+$ reactions (see Tables 3 and 4) seem to correlate with the $\Delta H$ values; they are slow for endothermic cases and the only fast reaction occurs for 2,3-dimethylheptane (exothermic by 8 kJ $mol^{-1}$).

Note that the adduct ions $M{\cdot}H_3O^+$ formed at the lower temperature of 300 K are highly reactive with $H_2O$ molecules and thus they may only be observed in a highly dry carrier gas for which even a few ppmv of water vapour causes their rapid conversion *via* ligand switching to the $H_3O^+H_2O$ secondary product ion.[34] At the higher temperature of 393 K, formation of the adducts is suppressed.[35]

**3.1.2. $NO^+$ reactions.** In contrast to the $H_3O^+$ reactions, these $NO^+$ reactions with alkanes proceed as hydride ion ($H^-$) transfer. The only exception is *n*-hexane, where fragment ions are observed along with minor adduct ions:

$$NO^+ + C_6H_{14} \rightarrow C_6H_{13}^+ + HNO \quad (m/z\ 85) \qquad (5a)$$

$$\rightarrow C_6H_{11}^+ + H_2 + HNO \quad (m/z\ 83) \qquad (5b)$$

$$\xrightarrow{He,N_2} C_6H_{14}NO^+ \quad (m/z\ 116) \qquad (5c)$$

Note that the rate coefficient for the reaction in He ($k$ = 0.1 × $10^{-9}$ $cm^3$ $s^{-1}$) is slower than in $N_2$ ($k$ = 0.7 × $10^{-9}$ $cm^3$ $s^{-1}$) (as shown in Table 4), because $N_2$ is a more effective

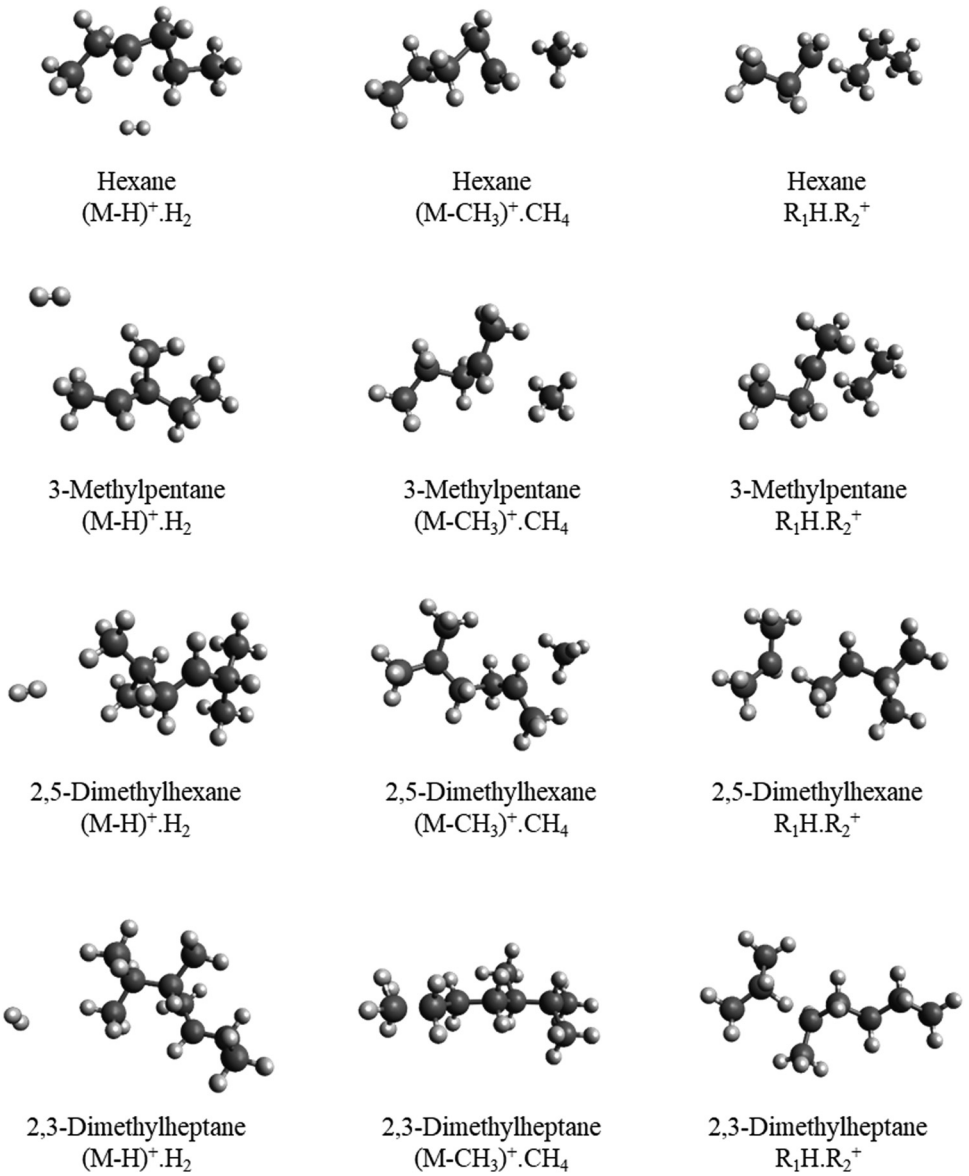


Fig. 3 Calculated structures of the different possible protonated arrangements of the four hydrocarbons studied in this work. Black spheres represent C atoms, and white spheres represent H atoms.

Table 5 The proton affinities (kJ mol$^{-1}$) calculated for the different possible stable structures of $MH^+$ ions are shown in Fig. 3

| PA (kJ mol$^{-1}$) | $(M–H)^+ \cdot H_2$ | $(M–CH_3)^+ \cdot CH_4$ | $R_1H \cdot R_2^+$ |
|---|---|---|---|
| *n*-Hexane | 678 | 677 | **693**[a] |
| 3-Methylpentane | 680 | **730** | **724** |
| 2,5-Dimethylhexane | **693** | **741** | **727** |
| 2,3-Dimethylheptane | **701** | 599 | **763** |

[a] The values greater than 691 kJ mol$^{-1}$ are indicated in bold.

Table 6 Enthalpy ($\Delta H$) and free energy ($\Delta G$) changes in the $H_3O^+$ reactions with hydrocarbons producing $(M–H)^+ + H_2 + H_2O$ products (reactions (2b), (3b) and (4a)), calculated by DFT

| Thermodynamics | $\Delta H$ (kJ mol$^{-1}$) | $\Delta G$ (kJ mol$^{-1}$) |
|---|---|---|
| *n*-Hexane | 13 | −23 |
| 3-Methylpentane | 11 | −25 |
| 2,5-Dimethylhexane | −3 | −37 |
| 2,3-Dimethylheptane | −8 | −37 |

third body for collisional stabilisation of the adduct ions. For 3-methylpentane, 2,5-dimethylhexane, and 2,3-dimethylheptane, the hydride ion transfer process was the only reaction observed:

$$NO^+ + C_6H_{14} \rightarrow C_6H_{13}^+ + HNO \quad (m/z\ 85) \qquad (6)$$

$$NO^+ + C_8H_{18} \rightarrow C_8H_{17}^+ + HNO \quad (m/z\ 113) \qquad (7)$$

$$NO^+ + C_9H_{20} \rightarrow C_9H_{19}^+ + HNO \quad (m/z\ 127) \qquad (8)$$

 

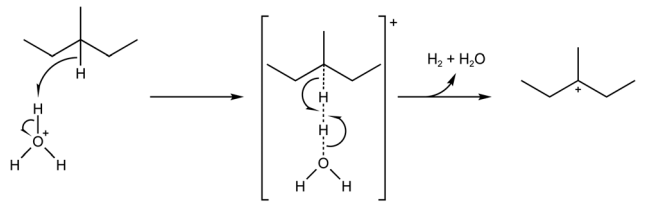


Fig. 4 The suggested mechanism of $(M-H)^+$ formation and $H_2$ ejection from the reaction of 3-methylpentane and the $H_3O^+$ reagent ion.

The present observation of hydride ion transfer as the major process is in agreement with previous work.[33,34] Note that the previous results for the $NO^+$ and *n*-hexane reaction showed only a slow hydride ion transfer reaction. However, the more accurate present study adds a 14% fragment and a 1% adduct, which were neglected previously.[34]

It is known that $NO^+$ ions may undergo charge transfer reactions[36] with molecules having ionisation energies (IE) lower than that of $NO^\bullet$, which is 9.25 eV. Thus, charge transfer was not observed in the $NO^+$ reactions with *n*-hexane, 3-methylpentane or 2,5-dimethylhexane that have an IE of 10.29 eV, 10.04 eV, and 9.76 eV, respectively. Also, the absence of charge transfer to 2,3-dimethylheptane indicates that the IE of this molecule is likely $>9.25$ eV.

**3.1.3. $O_2^{+\bullet}$ reactions.** As is common in most $O_2^{+\bullet}$ reactions with organic molecules, charge transfer was observed with alkanes *via* nondissociative formation of the molecular radical cation, in conjunction with multiple dissociative channels leading to various fragments (see Table 1).

$$O_2^{+\bullet} + C_nH_{2n+2} \rightarrow C_nH_{2n+2}^{+\bullet} + O_2 \quad (9a)$$

$$\rightarrow C_xH_y^+ + C_{n-x}H_{2n+2-y} + O_2 \quad (9b)$$

The percentage of the nondissociative channel varied widely between the compounds and significantly also between the experimental conditions. It is thus instructive to plot the percentages of the undissociated molecular radical cation product ($C_nH_{2n+2}^{+\bullet}$) for different carrier gases, temperatures and instrumental arrangements for extraction of the product ions from the flow tube. The branching ratios of channel (9a)

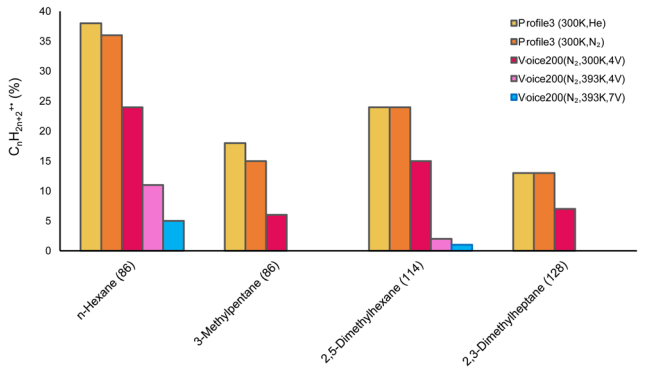


Fig. 5 The percentage of the nondissociative charge transfer from $O_2^{+\bullet}$ for each alkane under various conditions.

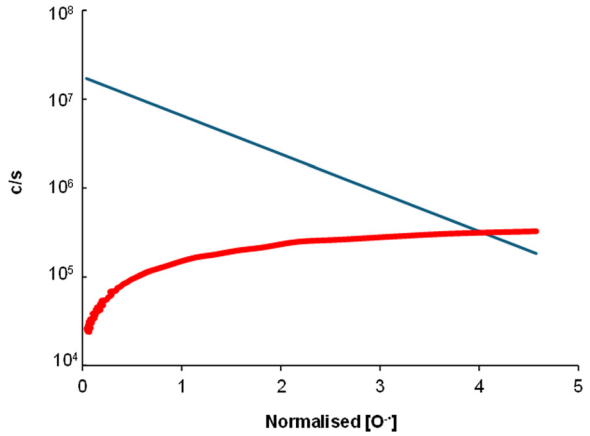


Fig. 6 Associative detachment process of 3-methylpentane demonstrated by the relative concentrations of $[O^{-\bullet}]$ at $m/z$ −16 (blue) and $[SF_6^-]$ at $m/z$ −146 (red).

under various conditions are illustrated in the bar chart in Fig. 5.

Amongst the compounds, the linear alkane (*n*-hexane) products exhibited the lowest percentage of fragmentation under He and $N_2$ at 300 K. However, a significant decrease in the branching ratio of reaction (9a) was observed under elevated temperatures (393 K) and higher extraction lens voltages (4 V and 7 V), indicating increased fragmentation. The branched structure of 3-methylpentane had a much greater degree of fragmentation. 2,5-Dimethylhexane had similar branching ratios for nondissociative charge transfer under He and $N_2$ at 300 K, but it decreased with increasing temperature and voltage. 2,3-Dimethylheptane exhibits the lowest values overall. In all cases, there is a clear trend in the Profile 3 where the branching ratios do not change between He or $N_2$; they decrease in the Voice200 due to the presence of additional electric fields;[37] and further reduce with increasing temperature and extraction lens voltage. The decreasing trend with the size of the alkane molecule agrees with the previous work, which also reported low proportions of the charge transfer product for larger alkanes.[34]

### 3.2. Negative ions

Out of the available negative ions in the Voice200infiinity, the only reagent that reacted significantly with the alkanes was $O^{-\bullet}$. No reactions were observed for $OH^-$, $O_2^{-\bullet}$, $NO_2^-$ or $NO_3^-$. The $O^{-\bullet}$ reactions proceed as associative detachment, as confirmed by $SF_6$ capturing free electrons; Fig. 6 shows an example of 3-methylpentane where the $SF_6^-$ product ion signal increases as the count rates of $O^{-\bullet}$ decrease.[38] The rate coefficients were estimated by comparison with the positive ion reactions to be in the range of 1 to 1.6 (in the units of $10^{-9}$ $cm^3$ $s^{-1}$).

## 4. Conclusion

Whilst alkanes are seemingly the simplest type of organic molecule, reactions of the SIFT-MS reagent ions with these

molecules exhibit an unexpected complexity. One of the most interesting results obtained in the present detailed study is that $H_3O^+$ does not transfer its proton to alkane molecules, even though the calculated proton affinities would indicate that this should be possible. Instead, product ions at $m/z$ (M-1) are formed alongside the adduct ions. Thus, the widely held concept within the SIFT-MS and PTR-MS communities[39] that $H_3O^+$ reacts with VOCs *via* fast proton transfer reactions[32,39] does not apply to alkanes. DFT-optimised lowest energy protonated structures do not correspond to a proton sitting on the molecule but instead involve the insertion of the proton between two C atoms, resulting in a complex with a hydrocarbon molecule ($CH_4$ or $C_3H_8$) and a closed-shell ion. DFT calculations further reveal that the reaction of $H_3O^+$ with alkanes producing $H_2$ and the $[M–H]^+$ product ions are near thermoneutral and substantially exergonic and are therefore entropically driven. This is accompanied by the finding that $H_3O^+$ ions undergo efficient association reactions with alkanes, producing $M{\cdot}H_3O^+$ adducts, indicating the formation of a long-lasting reaction complex. It is from this complex, that after appropriate rearrangement, $H_2$ is ejected together with $H_2O$; this is also suggested by exploratory molecular dynamics simulations, which would deserve dedicated future work outside the scope of the present study. The $M{\cdot}H_3O^+$ adducts undergo rapid ligand-switching reactions with $H_2O$ molecules forming $H_3O^+{\cdot}H_2O$ and will not thus be present on SIFT-MS spectra obtained in the presence of water vapour.

$NO^+$ reacted predominantly *via* hydride ion transfer, also forming $[M–H]^+$; the same product ion as $H_3O^+$, a rather unusual case amongst VOCs. Thus, in SIFT-MS applications, one way to identify alkanes is by observation of the same ions on $H_3O^+$ and $NO^+$ spectra. The $O_2^{+\bullet}$ reactions resulted in a variable amount of molecular radical cations and multiple fragment ions. The negative reagent ions did not lead to any product ions and are thus not useful for alkane SIFT-MS analyses.

## Data availability

The data supporting this article are available in the National Repository at **https://doi.org/10.48700/datst.gzx8g-3tt47** under the Creative Commons open access licence.

## Conflicts of interest

There are no conflicts to declare.

## Acknowledgements

The authors gratefully acknowledge financial support from the Czech Science Foundation (Grantová Agentura České Republiky, GACR; Project No. 21-25486S) and from the Praemium Academiae funding by the Czech Academy of Sciences. We would also like to thank Nicholas Demarais for his feedback.

## References

1 D. Smith, P. Španěl, N. Demarais, V. S. Langford and M. J. McEwan, Recent developments and applications of selected ion flow tube mass spectrometry (SIFT-MS), *Mass Spectrom. Rev.*, 2023, **n/a**, e21835, DOI: **10.1002/mas.21835**.
2 A. S. Lehnert, T. Behrendt, A. Ruecker, G. Pohnert and S. E. Trumbore, SIFT-MS optimization for atmospheric trace gas measurements at varying humidity, *Atmos. Meas. Technol.*, 2020, **13**, 3507–3520, DOI: **10.5194/amt-13-3507-2020**.
3 V. S. Langford, SIFT-MS: Quantifying the Volatiles You Smell and the Toxics You Don't, *Chemosensors*, 2023, **11**, 111.
4 G. Ozcan-Sinir, Detection of adulteration in extra virgin olive oil by selected ion flow tube mass spectrometry (SIFT-MS) and chemometrics, *Food Control*, 2020, **118**, 107433, DOI: **10.1016/j.foodcont.2020.107433**.
5 I. Belluomo, P. R. Boshier, A. Myridakis, B. Vadhwana, S. R. Markar, P. Spanel and G. B. Hanna, Selected ion flow tube mass spectrometry for targeted analysis of volatile organic compounds in human breath, *Nat. Protoc.*, 2021, **16**, 3419–3438, DOI: **10.1038/s41596-021-00542-0**.
6 J. La Nasa, I. Degano, F. Modugno, C. Guerrini, F. Facchetti, V. Turina, A. Carretta, C. Greco, E. Ferraris, M. P. Colombini and E. Ribechini, Archaeology of the invisible: the scent of Kha and Merit, *J. Archaeol. Sci.*, 2022, **141**, 105577, DOI: **10.1016/j.jas.2022.105577**.
7 C. Guerrini, F. Nardella, A. Morganti, J. La Nasa, I. Degano and E. Ribechini, Focusing on Volatile Organic Compounds of Natural Resins by Selected-Ion Flow Tube-Mass Spectrometry, *J. Am. Soc. Mass Spectrom.*, 2022, **33**, 1465–1473, DOI: **10.1021/jasms.2c00042**.
8 D. Smith, M. J. McEwan and P. Španěl, Understanding Gas Phase Ion Chemistry Is the Key to Reliable Selected Ion Flow Tube-Mass Spectrometry Analyses, *Anal. Chem.*, 2020, **92**, 12750–12762, DOI: **10.1021/acs.analchem.0c03050**.
9 D. Hera, V. S. Langford, M. J. McEwan, T. I. McKellar and D. B. Milligan, Negative Reagent Ions for Real Time Detection Using SIFT-MS, *Environments*, 2017, **4**, 16, DOI: **10.3390/environments4010016**.
10 H. O. T. Pye and G. A. Pouliot, Modeling the Role of Alkanes, Polycyclic Aromatic Hydrocarbons, and Their Oligomers in Secondary Organic Aerosol Formation, *Environ. Sci. Technol.*, 2012, **46**, 6041–6047, DOI: **10.1021/es300409w**.
11 M. P. Fraser, G. R. Cass, B. R. T. Simoneit and R. A. Rasmussen, Air Quality Model Evaluation Data for Organics. 4. C2–C36 Non-Aromatic Hydrocarbons, *Environ. Sci. Technol.*, 1997, **31**, 2356–2367, DOI: **10.1021/es960980g**.
12 E. Aghdassi and J. P. Allard, Breath alkanes as a marker of oxidative stress in different clinical conditions, *Free Radical Biol. Med.*, 2000, **28**, 880–886, DOI: **10.1016/S0891-5849(00)00189-1**.
13 A. V. Gossum and J. Decuyper, Breath alkanes as an index of lipid peroxidation, *Eur. Respir. J.*, 1989, **2**, 787, DOI: **10.1183/09031936.93.02080787**.
14 M. A. Pelli, G. Trovarelli, E. Capodicasa, G. E. De Medio and G. Bassotti, Breath alkanes determination in ulcerative colitis and Crohn's disease, *Dis. Colon Rectum*, 1999, **42**, 71–76, DOI: **10.1007/Bf02235186**.

 

15 M. Phillips, R. N. Cataneo, T. Cheema and J. Greenberg, Increased breath biomarkers of oxidative stress in diabetes mellitus, *Clin. Chim. Acta*, 2004, **344**, 189–194, DOI: 10.1016/j.cccn.2004.02.025.
16 R. J. Keogh and J. C. Riches, The Use of Breath Analysis in the Management of Lung Cancer: Is It Ready for Prime-time?, *Curr. Oncol. Rep.*, 2022, **29**, 7355–7378.
17 D. Smith and P. Španěl, Ternary association reactions of $H_3O^+$, $NO^+$ and $O_2^{+\bullet}$ with $N_2$, $O_2$, $CO_2$ and $H_2O$; implications for selected ion flow tube mass spectrometry analyses of air and breath, *Rapid Commun. Mass Spectrom.*, 2022, **36**, e9241, DOI: 10.1002/rcm.9241.
18 P. Španěl and D. Smith, Progress in SIFT-MS: breath analysis and other applications, *Mass Spectrom. Rev.*, 2011, **30**, 236–267, DOI: 10.1002/mas.20303.
19 D. Smith and P. Španěl, Ambient analysis of trace compounds in gaseous media by SIFT-MS, *Analyst*, 2011, **136**, 2009–2032, DOI: 10.1039/c1an15082k.
20 P. Španěl and D. Smith, Advances in On-line Absolute Trace Gas Analysis by SIFT-MS, *Curr. Anal. Chem.*, 2013, **9**, 525–539.
21 P. Španěl and D. Smith, Dissociation of $H_3O^+$, $NO^+$ and $O_2^{+\bullet}$ reagent ions injected into nitrogen carrier gas in SIFT-MS and reactivity of the ion fragments, *Int. J. Mass Spectrom.*, 2020, **458**, 116438, DOI: 10.1016/j.ijms.2020.116438.
22 K. Sovová, K. Dryahina and P. Španěl, Selected ion flow tube (SIFT) studies of the reactions of $H_3O^+$, $NO^+$ and $O_2^{+\bullet}$ with six volatile phytogenic esters, *Int. J. Mass Spectrom.*, 2011, **300**, 31–38, DOI: 10.1016/j.ijms.2010.11.021.
23 T. Su and W. J. Chesnavich, Parametrization of the ion–polar molecule collision rate constant by trajectory calculations, *J. Chem. Phys.*, 1982, **76**, 5183–5185, DOI: 10.1063/1.442828.
24 F. Neese, Software update: the ORCA program system---Version 5.0, *Wiley Interdiscip. Rev.: Comput. Mol. Sci.*, 2022, **12**, e1606, DOI: 10.1002/wcms.1606.
25 E. Caldeweyher, S. Ehlert, A. Hansen, H. Neugebauer, S. Spicher, C. Bannwarth and S. Grimme, A generally applicable atomic-charge dependent London dispersion correction, *J. Chem. Phys.*, 2019, **150**, 154122, DOI: 10.1063/1.5090222.
26 M. Bhatia, A DFT evaluation of molecular reactivity of volatile organic compounds in support of chemical ionization mass spectrometry, *Comput. Theor. Chem.*, 2023, **1223**, 114101, DOI: 10.1016/j.comptc.2023.114101.
27 M. Bhatia, Computational insights into phthalate ester-linked VOCs: a density functional theory (DFT)-based approach for chemical ionization mass spectrometry (CI-MS) analysis, *Rapid Commun. Mass Spectrom.*, 2024, **38**, e9863, DOI: 10.1002/rcm.9863.
28 S. J. Swift, N. Sixtova, M. Omezzine Gnioua and P. Španěl, A SIFT-MS study of positive and negative ion chemistry of the *ortho*-, *meta*- and *para*-isomers of cymene, cresol, and ethylphenol, *Phys. Chem. Chem. Phys.*, 2023, **25**, 17815–17827, DOI: 10.1039/d3cp02123h.
29 M. Omezzine Gnioua, A. Spesyvyi and P. Španěl, Gas phase $H^+$, $H_3O^+$ and $NH_4^+$ affinities of oxygen-bearing volatile organic compounds; DFT calculations for soft chemical ionisation mass spectrometry, *Phys. Chem. Chem. Phys.*, 2023, **25**, 30343–30348, DOI: 10.1039/D3CP03604A.
30 The National Institute of Standards and Technology (NIST) Chemistry WebBook, SRD 69, (https://webbook.nist.gov/).
31 F. Neese, Software update: the ORCA program system, version 4.0, *Wiley Interdiscip. Rev.: Comput. Mol. Sci.*, 2018, **8**, e1327, DOI: 10.1002/wcms.1327.
32 S. J. Swift, D. Smith, K. Dryahina, M. O. Gnioua and P. Španěl, Kinetics of reactions of $NH_4^+$ with some biogenic organic molecules and monoterpenes in helium and nitrogen carrier gases: a potential reagent ion for selected ion flow tube mass spectrometry, *Rapid Commun. Mass Spectrom.*, 2022, **36**, e9328, DOI: 10.1002/rcm.9328.
33 P. F. Wilson, C. G. Freeman and M. J. McEwan, Reactions of small hydrocarbons with $H_3O^+$, $O_2^+$ and $NO^+$ ions, *Int. J. Mass Spectrom.*, 2003, **229**, 143–149, DOI: 10.1016/S1387-3806(03)00290-2.
34 P. Španěl and D. Smith, Selected ion flow tube studies of the reactions of $H_3O^+$, $NO^+$, and $O_2^+$ with several aromatic and aliphatic hydrocarbons, *Int. J. Mass Spectrom.*, 1998, **181**, 1–10, DOI: 10.1016/S1387-3806(98)14114-3.
35 P. Španěl, S. J. Swift, K. Dryahina and D. Smith, Relative influence of helium and nitrogen carrier gases on analyte ion branching ratios in SIFT-MS, *Int. J. Mass Spectrom.*, 2022, **476**, 116835, DOI: 10.1016/j.ijms.2022.116835.
36 R. B. Michalcikova, K. Dryahina and P. Španěl, A detailed study of the ion chemistry of alkenes focusing on heptenes aimed at their SIFT-MS quantification, *Int. J. Mass Spectrom.*, 2018, **425**, 16–21, DOI: 10.1016/j.ijms.2017.12.004.
37 S. J. Swift, P. Spanel, N. Sixtová and N. Demarais, How to Use Ion-Molecule Reaction Data Previously Obtained in Helium at 300 K in the New Generation of Selected Ion Flow Tube Mass Spectrometry Instruments Operating in Nitrogen at 393 K, *Anal. Chem.*, 2023, **95**, 11157–11163, DOI: 10.1021/acs.analchem.3c02173.
38 D. Smith, P. Španěl, S. Matejcik, A. Stamatovic, T. D. Mark, T. Jaffke and E. Illenberger, Formation of $SF_5^-$ in electron-attachment to $SF_6^-$ swarm and beam results reconciled, *Chem. Phys. Lett.*, 1995, **240**, 481–488.
39 T. Reinecke, M. Leiminger, A. Jordan, A. Wisthaler and M. Müller, Ultrahigh Sensitivity PTR-MS Instrument with a Well-Defined Ion Chemistry, *Anal. Chem.*, 2023, **95**, 11879–11884, DOI: 10.1021/acs.analchem.3c02669.